



Title	Ice flow and isostasy of the north polar cap of Mars
Author(s)	Greve, Ralf; Klemann, Volker; Wolf, Detlef
Citation	Planetary and Space Science, 51(3), 193-204 https://doi.org/10.1016/S0032-0633(02)00206-4
Issue Date	2003-03
Doc URL	http://hdl.handle.net/2115/35491
Type	article (author version)
File Information	Greve_etal_2003_PSS.pdf



[Instructions for use](#)

Ice flow and isostasy of the north polar cap of Mars

RALF GREVE (1), VOLKER KLEMMANN (2),
and DETLEF WOLF (2)

(1) Fachbereich Mechanik, Technische Universität Darmstadt,
Hochschulstraße 1, D-64289 Darmstadt, Germany

(2) GeoForschungsZentrum Potsdam, Abteilung 1: Kinematik und Dynamik der Erde,
Telegrafenberg, D-14473 Potsdam, Germany

March 15, 2003

Correspondence to: R. Greve (greve@mechanik.tu-darmstadt.de)

Abstract

The flow of the north polar cap of Mars, which is assumed to consist mainly of H₂O ice, is investigated with the three-dimensional ice-sheet model SICOPOLIS. We consider a simplified topography and a climatic forcing varying between the present state and warmer, more humid conditions in the past with an obliquity cycle of 1.3 million earth years (yr). Furthermore, SICOPOLIS is coupled with the three-layer viscoelastic ground model `displace` to simulate the isostatic response of the underlying lithosphere/mantle system. Likely ice-flow velocities at present are a few mm/yr, along with surface accumulation/ablation rates of the order of 0.1 mm water equiv./yr and basal temperatures more than 50°C below pressure melting. Thicknesses of the rheological lithosphere of 50–400 km are consistent with geothermal heat fluxes of 15–36 mW m⁻², with some evidence for values of ca. 80–120 km and 20–30 mW m⁻², respectively. For an Earth-like upper-mantle viscosity of $\mathcal{O}(10^{21}$ Pa s), relaxation times of the lithosphere/mantle system are much shorter than significant load changes, so that the mantle behaves as an inviscid fluid. The poor correlation between the computed and measured free-air gravity signal indicates that it is determined by mass anomalies of a different origin.

1 Introduction

Both Martian poles are covered by surface ice caps, which vary considerably over the seasons. During the respective winter, these surface caps extend toward the equator beyond 55°N/S, whereas, in the summer, only much smaller residual ice caps survive within 80°N/S. Whereas the seasonal caps consist of a thin layer of CO₂ snow, perhaps some 10 cm thick, the Mars Orbiter Laser Altimeter (MOLA) measurements of the Mars Global Surveyor (MGS) spacecraft revealed that the complexes composed of the residual caps and the underlying polar layered deposits are massive topographic structures, which rise about 3 km above the surroundings (Zuber *et al.* 1998, Smith *et al.* 1999a; Fig. 1a). Throughout this paper, we will refer to these complexes as the *north* and *south polar cap*, respectively, following the terminology of many recent publications (e.g., Johnson *et al.* 2000, Byrne and Murray 2002). The polar caps serve as cold traps for atmospheric water and highly likely consist of H₂O ice with an unknown amount of mixed-in dust (Clifford *et al.* 2000). Therefore, they form small inland ice sheets in the meaning of terrestrial glaciology.

In a previous study by Greve (2000a), dynamic/thermodynamic model simulations were carried out for the north polar cap (NPC), approximated, for simplicity, as a paraboloid-like cap with volume, area and maximum thickness equal to those of the actual NPC. The NPC was investigated for three climate scenarios: present steady-state conditions or

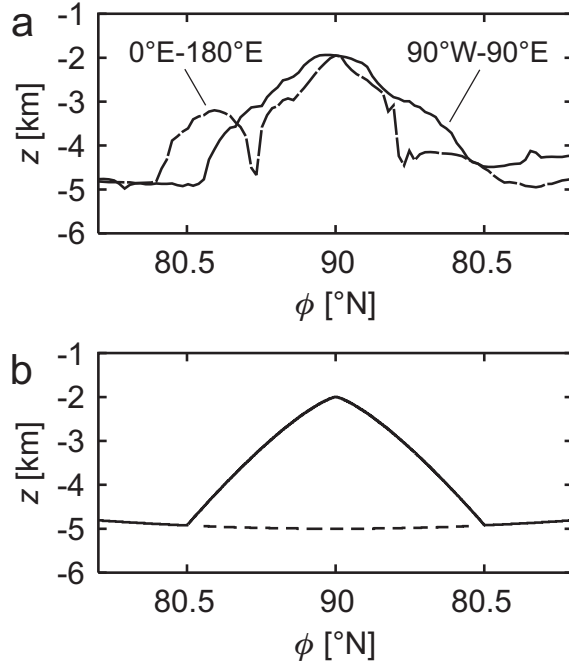


Figure 1: (a) Transects of the MOLA topography of the present NPC along meridians 90°W - 90°E and 0°E - 180°E (resolution 20 km). (b) Simplified paraboloid topography (solid: surface, dashed: equilibrated ground) according to Eqs. (6) and (7). The actual ground will be lowered according to the isostatic compensation of the ice load.

periodically varying conditions between cold and arid at present and warmer and more humid in the past with periods of either 125 kyr or 1.3 Myr (where yr stands for Earth years), which are the main periods of obliquity variations (Kieffer and Zent 1992). It was found that the 1.3-Myr cycle is most likely responsible for oscillations of the ice extent between the present margin and a larger extent south to 75°N indicated by ice remnants (Zuber *et al.* 1998).

Here, we take up this result and extend the previous work by coupling the model of the NPC with a model of the dynamics of the underlying lithosphere/mantle system. Apart from investigating the major ice-dynamical questions of whether the NPC shows significant ice flow and whether the ice temperature allows for the presence of subglacial liquid water as a potential habitat for lifeforms, our aims are to constrain the present thickness of the rheological lithosphere and the geothermal heat flux, to compute the gravity anomaly due to the NPC and its compensation and to demonstrate that the gravity anomaly measured by orbit tracking of the MGS spacecraft results mainly from different sources such as mass anomalies in the ground. The latter finding confirms the results reported by Johnson *et al.* (2000).

Our central presumption is that the NPC is a dynamic H_2O ice mass with physical properties comparable to those of the terrestrial ice sheets and, therefore, controlled by

accumulation, ablation and glacial flow. This approach is controversial. Alternatively, one may argue that the NPC is a remnant of ancient, much larger ice masses, eroding away in the course of time without significant mass supply and flow. However, the absence of craters with diameters > 300 m indicates a low surface age of ≤ 100 kyr (Herkenhoff and Plaut, 2000). Also, vanishing H₂O-ice accumulation at the surface is not likely (Clifford *et al.* 2000) and does not agree with albedo and imaging data (Bass and Paige 1999). Finally, our understanding of the physical properties of H₂O ice requires the occurrence of glacial flow under the conditions that prevail for the NPC (Greve 2000a, Nye 2000).

2 Modelling approach

2.1 Ice-sheet model

The dynamic/thermodynamic behaviour of the NPC of Mars is investigated with the ice-sheet model SICOPOLIS (SIMulation COde for POLythermal Ice Sheets), which was originally developed for terrestrial ice sheets like Greenland, Antarctica and the glacial northern hemisphere [cf. Greve (2000b) and references therein]. The model describes the material ice as an incompressible, heat-conducting, power-law fluid with thermo-mechanical coupling due to the strong temperature dependence of the ice viscosity:

$$\mathbf{D} = EA(T')\sigma^{n-1} \mathbf{t}^D, \quad (1)$$

where $\mathbf{D} = \text{sym grad } \mathbf{v}$ (velocity \mathbf{v}) is the strain-rate tensor, \mathbf{t}^D the Cauchy stress deviator, $\sigma = [\text{tr}(\mathbf{t}^D)^2/2]^{1/2}$ the effective shear stress, n the power-law exponent, $A(T')$ the flow-rate factor [which depends exponentially on the temperature T' relative to the pressure melting point, see Greve *et al.* (1998)], and E the flow-enhancement factor, which is equal to unity for pure ice and can deviate from unity due to the softening or stiffening effect of impurities in the ice. It is further distinguished between *cold ice* with a temperature below the pressure melting point and *temperate ice* with a temperature at the pressure melting point, the latter being considered as a binary mixture of ice and small amounts of water. The interface that separates cold and temperate ice is monitored using Stefan-type energy flux and mass flux matching conditions.

The model computes the three-dimensional temporal evolution of ice extent, thickness, velocity, temperature, water content and age in response to external forcing. The latter must be specified by (i) the mean annual air temperature at the ice surface, (ii) the surface mass balance, which is ice accumulation (snowfall, condensation) minus ablation (melting, sublimation, erosion), (iii) the global sea level (not relevant for Martian applications)

and (iv) the geothermal heat flux entering the ice mass from below. However, for the simulations carried out in this study, instead of specifying the surface mass balance and computing the resulting topography evolution, the latter is prescribed, and the surface mass balance is computed such that it is consistent with the changing topography and the ice velocity field. This inverse approach has already been employed by Greve (2000a) and is pursued, because the MOLA data mentioned above have provided a very precise present topography of the NPC and an indication of its former extension (Zuber *et al.* 1998), whereas for present and past accumulation/ablation rates no direct measurements are available. The values of the relevant physical parameters used for the ice-sheet model are listed in Table 1.

Parameter	Value
Gravity, $g = g^{(0)}$	3.72 m s^{-2}
Density of ice, ρ_i	910 kg m^{-3}
Power-law exponent, n	3
Flow-enhancement factor, E	3
Heat conductivity of ice, λ_i	$9.828 e^{-0.0057 T[\text{K}]} \text{ W m}^{-1} \text{ K}^{-1}$
Specific heat of ice, c_i	$(146.3 + 7.253 T[\text{K}]) \text{ J kg}^{-1} \text{ K}^{-1}$
Latent heat of ice, L_i	335 kJ kg^{-1}
Clausius-Clapeyron gradient, β	$3.3 \cdot 10^{-4} \text{ K m}^{-1}$

Table 1: Values of the physical parameters used for the ice-sheet model.

2.2 Ground model

The isostatic response of the lithosphere due to the temporally varying ice load is simulated with the plain n -layer ground model `displace` (Wolf 1985a, Klemann and Wolf 1999). In the version used in this study, the incremental momentum equation applies to a continuum with hydrostatic pre-stress advection but without internal buoyancy (Wolf 1985b),

$$\text{div } \mathbf{t}^{(\delta)} + \text{grad } (\rho^{(0)} \mathbf{g}^{(0)} \cdot \mathbf{u}) = \mathbf{0}, \quad (2)$$

with $\mathbf{t}^{(\delta)}$ the material increment of the Cauchy stress tensor, $\rho^{(0)}$ the mass density in the reference state, $\mathbf{g}^{(0)}$ the constant reference gravity directed vertically downward and \mathbf{u} the displacement. In each layer, the material parameters are assumed to be homogeneous. The rheology of the continuum is that of a Maxwell-viscoelastic fluid,

$$\mathbf{t}^{(\delta)} = (\kappa \text{tr } \mathbf{e}) \mathbf{1} + 2 \int_0^t m(t - \check{t}) \frac{d\mathbf{e}^D}{d\check{t}} d\check{t}, \quad (3)$$

where $\mathbf{e} = \text{sym grad } \mathbf{u}$ is the infinitesimal strain tensor, \mathbf{e}^D the corresponding deviator, κ the elastic bulk modulus and

$$m(t - \tilde{t}) = \mu e^{-\frac{\mu}{\eta}(t-\tilde{t})} \quad (4)$$

the shear-relaxation function for a Maxwell fluid expressed in terms of its elastic shear modulus μ and steady-state viscosity η .

The incremental gravity is calculated from the incremental Poisson equation,

$$\text{div grad } \phi^{(\Delta)} = 4\pi\gamma\rho^{(0)} \text{tr } \mathbf{e}, \quad (5)$$

with $\phi^{(\Delta)}$ the local increment of the potential at the reference height and γ the gravitational constant. The free-air gravity increment is $\mathbf{g}^{(\Delta)} = \text{grad } \phi^{(\Delta)}$ and the geoid displacement is given by $h_g = \phi^{(\Delta)}/g^{(0)}$ (Bruns formula; h_g positive upward, $g^{(0)}$ is the magnitude of $\mathbf{g}^{(0)}$). For the axisymmetric problem considered here, the incremental field equations (2)–(5) are solved in the Hankel-wave-number, k , and Laplace-frequency, s , domains, where they reduce to a system of ordinary differential equations in terms of the vertical coordinate, z . After consideration of the ice load, the results are transformed back to the space-time domain by evaluating the inverse Laplace and Hankel transforms. Because the ice-surface topography is taken with respect to a reference plane, see Sect. 2.1, the additional ice volume between this plane and the deformed ground must be considered as an additional load.

The stratification of the ground model consists of an elastic crust of thickness H_c , an elastic mantle lithosphere of thickness H_{ml} (which, together, form the rheological lithosphere of thickness $H_l = H_c + H_{ml}$) and a viscoelastic upper mantle below the lithosphere. The parameter values used for the ground model are given in Table 2 (Sohl and Spohn 1997, Spohn *et al.* 1998). Note that the lithosphere layers are treated as elastic ($\eta_c = \eta_{ml} = \infty$), whereas the upper mantle below the mantle lithosphere is treated as incompressible ($\kappa_{um} = \infty$) in order to keep the viscoelastic fluid stable (Klemann *et al.* 2003).

The most crucial parameter of the lithosphere/mantle system, the lithosphere thickness H_l , is varied between 50 and 400 km. These values cover the range of thicknesses discussed in the literature (Spohn *et al.* 1998, Johnson *et al.* 2000, Zuber *et al.* 2000).

Layer	Parameter	Value
Crust	Density, ρ_c	2900 kg m ⁻³
	Thickness, H_c	40 km
	Bulk modulus, κ_c	106.4 GPa
	Shear modulus, μ_c	44.8 GPa
	Viscosity, η_c	∞
Mantle lithosphere	Density, ρ_{ml}	3500 kg m ⁻³
	Thickness, H_{ml}	10 . . . 360 km
	Bulk modulus, κ_{ml}	136.3 GPa
	Shear modulus, μ_{ml}	74 GPa
	Viscosity, η_{ml}	∞
Upper mantle below lithosphere	Density, ρ_{um}	3500 kg m ⁻³
	Thickness, H_{um}	∞
	Bulk modulus, κ_{um}	∞
	Shear modulus, μ_{um}	145 GPa
	Viscosity, η_{um}	10 ²¹ Pa s

Table 2: Values of the physical parameters used for the ground model.

3 Model input

3.1 Topography

In the absence of any ice load, the isostatically equilibrated ground is approximated by a parabolic bowl,

$$z = b_0(r) = b_0^{90N} + (b_0^{30N} - b_0^{90N}) \frac{r^2}{R_b^2}, \quad (6)$$

where z is positive upward and equal to zero for the reference geoid, r the distance from the north pole (90°N) in the horizontal plane, $b_0^{90N} = -5$ km the elevation of the equilibrated ground at the pole, $b_0^{30N} = -2$ km the elevation of the equilibrated ground at 30°N, and $R_b = 3556.28$ km the distance from the pole to 30°N (Greve 2000a). The bowl approximates the MOLA data by Zuber *et al.* (1998) and is assumed to hold also below the NPC. The actual ground position, $z = b(r, t)$, then follows from $b = b_0 - w$, where w is the vertical surface displacement of the lithosphere (positive downward) due to glacial loading. The ice thickness above the equilibrated ground, $H^*(r, t)$, is described as a paraboloid-like cap,

$$H^*(r, t) = H_i(t) \left(1 - \left(\frac{r}{R_i(t)} \right)^{4/3} \right), \quad \text{for } r < R_i(t), \quad (7)$$

where the radius of the NPC varies harmonically in time, t ,

$$R_i(t) = \frac{R_i^0 + R_i^{\max}}{2} - \frac{R_i^{\max} - R_i^0}{2} \cos \frac{2\pi t}{t_{\text{obl}}}, \quad (8)$$

between the present ($t = 0$) minimum, $R_i^0 = 564.19$ km, and the past maximum, $R_i^{\max} = 889.07$ km. These values correspond to southward extents of the NPC to 80.5°N and 75°N , respectively. The symbol $t_{\text{obl}} = 1.3$ Myr denotes the period of the first modulation of the obliquity cycle, which was found to be the most likely period for significant climate-induced changes of the ice extent in the geologically recent past (Greve 2000a; Figs. 1, 2).

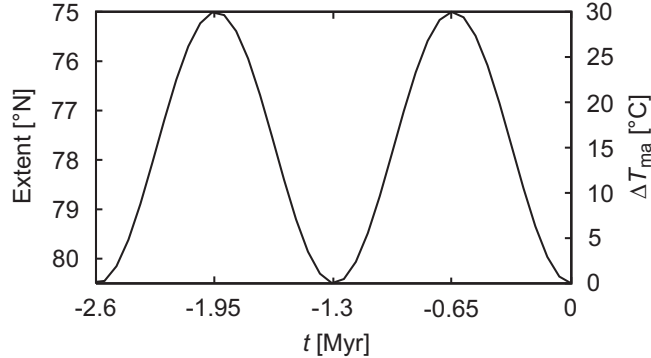


Figure 2: Simulation forcing: Ice extent and deviation of actual surface temperature from present surface temperature (same curve) over two 1.3 Myr obliquity cycles according to Eqs. (8) and (12).

The maximum thickness, $H_i(t)$, is calculated with the present value, $H_i^0 = 3$ km, and the assumption that

$$\frac{H_i^2(t)}{R_i(t)} = \text{const}, \quad (9)$$

which holds exactly for a perfectly plastic circular ice sheet on a rigid horizontal base (Paterson 1994). We thus obtain

$$H_i(t) = H_i^0 \left(\frac{R_i(t)}{R_i^0} \right)^{1/2}. \quad (10)$$

For the maximum radius assumed for the past, $R_i(t) = R_i^{\max}$, this yields a maximum thickness of $H_i^{\max} = 3.766$ km. In contrast, Greve (2000a) applied the ad-hoc assumption $H_i(t)/R_i(t) = \text{const}$, which corresponds to the larger value of $H_i^{\max} = 4.728$ km.

The simple representation of the topography by Eqs. (6)–(10) means that small- and medium-scale features of the present NPC like the 500 km long chasm and the spiraling troughs (Thomas *et al.*, 1992) are not accounted for. While these features are interesting and their origin is poorly understood, they are beyond the scope of this study which is the investigation of very basic, large-scale properties of the NPC and the underlying ground only.

3.2 Surface temperature

Following Greve (2000a) and references therein, we parameterize the present mean annual air temperature at the surface of the NPC, T_{ma} , as a linear function depending on co-latitude, $\tilde{\phi}$ ($\tilde{\phi} = 90^\circ\text{N} - \phi$, where ϕ is the latitude), and elevation, h ,

$$T_{\text{ma}}^{\text{present}}(\tilde{\phi}, h) = T_{\text{ma}}^0 + \gamma_{\text{ma}} h + c_{\text{ma}} \tilde{\phi}, \quad (11)$$

with the constants $T_{\text{ma}}^0 = -105^\circ\text{C}$, $\gamma_{\text{ma}} = -2.5^\circ\text{C}/\text{km}$ (mean lapse rate), and $c_{\text{ma}} = 1.5^\circ\text{C}/^\circ\text{lat}$. The difference from present conditions is described by the time-dependent offset

$$\Delta T_{\text{ma}}(t) = \frac{\Delta T_{\text{ma}}^{\text{max}}}{2} \left(1 - \cos \frac{2\pi t}{t_{\text{obl}}} \right), \quad (12)$$

which varies with the same obliquity period of $t_{\text{obl}} = 1.3$ Myr as the ice extent and thickness (see above) and has a maximum of $\Delta T_{\text{ma}}^{\text{max}} = 30^\circ\text{C}$ for periods of large obliquity (Fig. 2). Consequently, the space- and time-dependent surface-temperature forcing is

$$T_{\text{ma}}(\tilde{\phi}, h, t) = T_{\text{ma}}^{\text{present}}(\tilde{\phi}, h) + \Delta T_{\text{ma}}(t). \quad (13)$$

According to Eqs. (8), (10) and (12), minimum temperature corresponds to minimum ice volume and maximum temperature to maximum ice volume. The idea behind this somewhat counter-intuitive correlation (at least for terrestrial glaciologists) is that increasing air temperature entails increasing humidity and therefore a larger potential for precipitation, which builds up the NPC. On Earth, this effect is over-compensated by increased surface melting, which, however, is not relevant for the recent climate history of Mars due to the low temperatures. On Mars, ablation at the surface of the NPC is mainly due to sublimation of water ice into the atmosphere. Jakosky *et al.* (1993) modelled this process and found a strong increase of sublimation with increasing obliquity/surface temperature. This works against the increasing precipitation, and therefore the net effect on the surface mass balance is not clear from the outset. The reason to assume a positive correlation between surface temperature and ice volume is that otherwise the ice volume would be maximal at present, which does not agree with a larger extent south to 75°N in the past. Temperature and ice volume are assumed to follow the first modulation (period of $t_{\text{obl}} = 1.3$ Myr) of the obliquity cycle, which is currently close to its minimum (Ward 1992), in phase, so that both quantities are minimal at present (Greve 2000a).

Touma and Wisdom (1993) and Laskar *et al.* (2002) pointed out that the obliquity, which, as mentioned above, currently oscillates with periods of 125 kyr and 1.3 Myr between ca. 15° and 35° around the average of 25° , probably underwent a transition about

4 Myr ago, with a ca. 10° larger average obliquity before that time. Since this shift must have been associated with a significant shift in the climatic conditions which is not reflected by our scenario of temperature and ice volume, we restrict our study to the period from 2.6 Myr ago until the present, that is, the two most recent long obliquity cycles.

Of course, the response of the climate system to harmonic orbital forcing is not necessarily harmonic due to the nonlinear nature of the system. Therefore, the assumed harmonic temperature and ice-volume variations described by Eqs. (8), (10) and (12) are only an approximation owing to the lack of better knowledge about the generation of higher-frequency responses of the climate system. Again, considering the very fundamental objective of this study, this is not a severe problem.

3.3 Geothermal heat flux

The geothermal heat flux at the top of the crust in the north polar region, $q_{\text{geo}}^{\text{s}}$, is a crucial parameter for the ice flow, because it largely controls the temperature field in the lower parts of the NPC. Via the exponentially temperature-dependent flow-rate factor $A(T')$ in Eq. (1), this has a pronounced effect on the ice viscosity and therefore on the flow velocity. Here, we vary the geothermal heat flux between 10 and 50 mW m^{-2} . This is based on published estimates based on models of the Martian interior (e.g., Solomon and Head 1990, Schubert *et al.* 1992, Sohl and Spohn 1997, Wüßner and Harder 1998).

Layer	Parameter	Value
Crust	Heat conductivity, λ_{c}	$2.5 \text{ W m}^{-1} \text{ K}^{-1}$
	Heat source density, r_{c} (depleted)	$2.5 \times 10^{-9} \text{ W m}^{-3}$
	Heat source density, r_{c} (enriched)	$3.9 \times 10^{-7} \text{ W m}^{-3}$
Mantle lithosphere	Heat conductivity, λ_{ml}	$4 \text{ W m}^{-1} \text{ K}^{-1}$
	Heat source density, r_{ml}	$2.5 \times 10^{-9} \text{ W m}^{-3}$

Table 3: Values of the physical parameters for the geothermal heat flux model.

With some further assumptions, the geothermal heat flux can be related to the thickness of the rheological lithosphere, H_1 . To this end, we use the parameter values of Table 3. The given values for the heat conductivities of the crust and the mantle lithosphere, λ_{c} and λ_{ml} , respectively, are based on results by Solomon and Head (1990). The range of heat source densities, r_{c} and r_{ml} , is by Wüßner and Harder (1998). As for r_{c} , these authors assume an old southern-hemispheric crust formed by differentiation of an early mantle and therefore enriched by radiogenic isotopes, and, in contrast, a younger northern-hemispheric crust formed by a depleted mantle (see also Breuer *et al.* 1993). Consequently, the depleted

crust is more likely for the region of the NPC. Nevertheless, we consider both values as limits of a possible range.

The mean temperature at the top of the crust is set to $T_s = 193$ K (-80°C). To assess the base of the rheological lithosphere, we use the proposed isotherm $T_1 = 0.6 \times T_{\text{melt}}$ (Meissner and Vetter 1979). The melting temperature of the upper-mantle material, T_{melt} , at the depth H_1 is computed according to terrestrial conditions by

$$p [\text{GPa}] = \frac{T_{\text{melt}} [\text{K}] - 1373}{136} + 4.968 \times 10^{-4} \exp [1.2 \times 10^{-2} (T_{\text{melt}} [\text{K}] - 1373)] \quad (14)$$

(McKenzie and Bickle 1988), where $p = \rho_c g H_c + \rho_{\text{ml}} g H_{\text{ml}}$ is the hydrostatic pressure at the base of the lithosphere (see Table 2).

Let \tilde{z} be the vertical coordinate, positive downward and equal to zero at the top of the crust (this is different from the definition of z in Sect. 3.1). Then, in the crust,

$$q_{\text{geo}}(\tilde{z}) = q_{\text{geo}}^s - r_c \tilde{z} = \lambda_c \frac{\partial T}{\partial \tilde{z}}, \quad (15)$$

so that

$$T(\tilde{z}) = T_s + \frac{q_{\text{geo}}^s}{\lambda_c} \tilde{z} - \frac{r_c}{2\lambda_c} \tilde{z}^2. \quad (16)$$

In an analogous way, in the mantle lithosphere,

$$q_{\text{geo}}(\tilde{z}) = q_{\text{geo}}^{c/m} - r_{\text{ml}}(\tilde{z} - H_c) = \lambda_{\text{ml}} \frac{\partial T}{\partial \tilde{z}} \quad (17)$$

(the index “c/m” refers to the crust/mantle boundary at the depth $\tilde{z} = H_c$), which yields with Eqs. (15) and (16)

$$\begin{aligned} T(\tilde{z}) &= T_{c/m} + \frac{q_{\text{geo}}^{c/m}}{\lambda_{\text{ml}}}(\tilde{z} - H_c) - \frac{r_{\text{ml}}}{2\lambda_{\text{ml}}}(\tilde{z} - H_c)^2 \\ &= T_s + \frac{q_{\text{geo}}^s}{\lambda_c} H_c - \frac{r_c}{2\lambda_c} H_c^2 + \frac{q_{\text{geo}}^s - r_c H_c}{\lambda_{\text{ml}}}(\tilde{z} - H_c) - \frac{r_{\text{ml}}}{2\lambda_{\text{ml}}}(\tilde{z} - H_c)^2. \end{aligned} \quad (18)$$

This temperature profile holds for the entire thermal lithosphere in which heat transport is controlled by conduction. The above definition of the base of the rheological lithosphere corresponds to the condition

$$T(\tilde{z} = H_1) = T_1. \quad (19)$$

Inserting this into Eq. (18) gives

$$T_1 = T_s + q_{\text{geo}}^s \left(\frac{H_c}{\lambda_c} + \frac{H_1 - H_c}{\lambda_{\text{ml}}} \right) - \frac{r_c H_c (H_1 - H_c)}{\lambda_{\text{ml}}} - \frac{r_{\text{ml}} (H_1 - H_c)^2}{2\lambda_{\text{ml}}} - \frac{r_c H_c^2}{2\lambda_c} \quad (20)$$

or, solved for q_{geo}^s ,

$$q_{\text{geo}}^s = \left(T_1 - T_s + \frac{r_c H_c (H_1 - H_c)}{\lambda_{\text{ml}}} + \frac{r_{\text{ml}} (H_1 - H_c)^2}{2\lambda_{\text{ml}}} + \frac{r_c H_c^2}{2\lambda_c} \right) \times \left(\frac{H_c}{\lambda_c} + \frac{H_1 - H_c}{\lambda_{\text{ml}}} \right)^{-1}. \quad (21)$$

This equation relates the geothermal heat flux at the top of the crust to the thickness of the rheological lithosphere. Results are shown in Fig. 3 for the depleted and the enriched crust. Evidently, q_{geo}^s decreases with increasing H_1 , and the assumed interval $H_1 = 50 \dots 400$ km corresponds approximately to $q_{\text{geo}}^s = 45 \dots 10 \text{ mW m}^{-2}$. However, since the above parameter values required to derive this relation are rather uncertain, we only use it as an additional confirmation for the consistency of our investigated ranges $H_1 = 50 \dots 400$ km, $q_{\text{geo}}^s = 10 \dots 50 \text{ mW m}^{-2}$ and consider these two quantities as independent in the following.

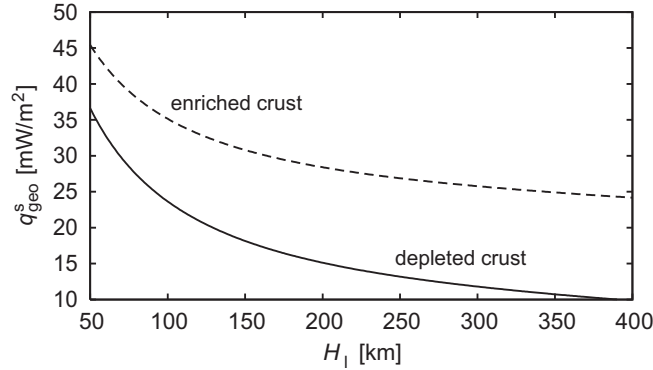


Figure 3: Computed geothermal heat flux at the top of the crust, q_{geo}^s , as a function of lithosphere thickness, H_1 , for heat source densities of a depleted (northern-hemisphere type) and an enriched (southern-hemisphere type) crust due to relation (21).

4 Discussion of simulations

4.1 Simulation set-up

For this study, a series of simulations with varied lithosphere thickness and geothermal heat flux was carried out. The model time for the simulations runs from $t = -2.6 \text{ Myr} = -2t_{\text{obl}}$ until $t = 0$ (present). Thus, two long obliquity cycles are covered. This guarantees that during the last cycle (on which we focus our attention) the results are independent of any arbitrary initial conditions. The time-dependent forcings of topography, surface temperature and geothermal heat flux are those described in Sect. 3. For the thickness of the rheological lithosphere, H_1 , the values 50, 100, 150, \dots , 400 km are used, and the geothermal heat flux, q_{geo}^s , is varied over the range 10, 15, 20, \dots , 50 mW m^{-2} .

4.2 Results

First, we assess the possible effect of viscoelasticity of the ground. Figure 4 shows the relaxation time of the three-layer lithosphere/mantle system, τ , as a function of the normalized Hankel wave number of the ice load, kR_m (where $R_m = 3397 \text{ km}$ is the mean Martian radius), for different values of H_1 . Two different modes appear: the buoyancy mode M0, which is mainly responsible for the vertical lithosphere displacement and the associated gravity signal, and the viscoelastic mode L0 with much smaller amplitudes (Wu and Peltier 1982, Wolf 1985a). For both modes and all values of H_1 , the relaxation times, τ , are always smaller than 30 kyr (1/40 of the obliquity period) for $kR_m \sim 10 \dots 20$ (approximately corresponding to the wavelengths of the ice load at maximum and minimum extent, respectively). Therefore, the lithosphere/mantle system follows the slowly varying ice load in a quasi-static fashion, which means that the finite viscosity of the upper mantle does not affect the dynamics of the system, and the material can be replaced by an inviscid fluid (what is done in our computations of lithosphere displacements). Of course, this result depends on the viscosity value assumed for the upper mantle. If it were larger than the terrestrial value of 10^{21} Pa s (Table 2) by at least an order of magnitude, the relaxation times would increase correspondingly and invalidate this reasoning. However, 10^{21} Pa s has turned out to be more like an upper bound for the dynamic viscosity in convection models recently discussed for Mars (e.g., Parmentier and Grasset 1998). Therefore, modelling the mantle as an inviscid fluid is justified.

By employing a similar viscoelastic lithosphere/mantle model, Johnson *et al.* (2000) report a relaxation time of 100 kyr for isostatic compensation, which they misleadingly named “Maxwell time”.¹ It is not completely clear how this figure was obtained. In

¹The Maxwell time describes the relaxation of shear stress and is the ratio of viscosity and shear

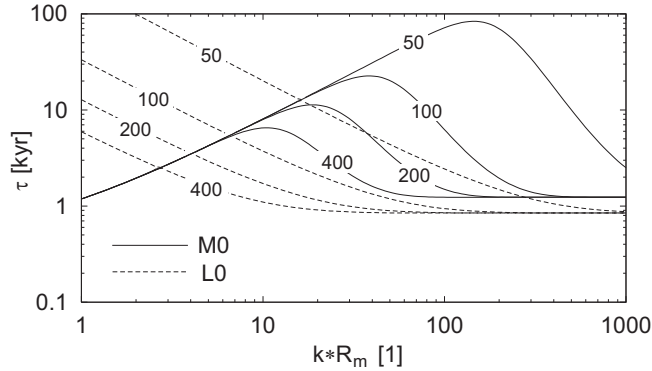


Figure 4: Relaxation time, τ , as a function of Hankel wave number of the ice load, k , normalized with respect to the mean Martian radius, R_m , for modes M0, L0 and lithosphere thicknesses of $H_1 = 50$ km, 100 km, 200 km, 400 km (labels on the lines).

any case, their Fig. 8 shows that relaxation times, understood like here as times required for reaching a fraction $(1 - 1/e) \approx 63\%$ of steady-state compensation, are ≤ 40 kyr for lithosphere thicknesses of 50–100 km and loads comparable in wavelength to the NPC, which agrees well with our findings.

In order to compare the isostatic responses of the different simulations, we define the fraction of isostatic compensation,

$$f_{\text{iso}} = \frac{w}{H \rho_i / \rho_{\text{um}}}, \quad (22)$$

which relates the actual surface displacement, w , to full isostatic compensation, which is local ice thickness, H , times the density ratio of ice and upper mantle, $\rho_i / \rho_{\text{um}}$. Fig. 5 shows f_{iso} for the centre of the NPC (north pole) and the two time slices $t = 0$ (present, minimum ice extent and thickness) and $t = -650$ kyr (half a cycle ago, maximum ice extent and thickness). Since, for our prescribed-topography scenarios, f_{iso} does not depend on q_{geo}^s , it is plotted only against H_1 .

It is evident that f_{iso} decreases strongly with increasing H_1 , for the present NPC (minimum extent) from more than 0.8 to less than 0.2 for the considered range of values of H_1 . Of course, this is so because the flexural rigidity of the elastic lithosphere becomes larger for larger values of H_1 (in the thin-plate approximation with the third power). In the range $H_1 \leq 200$ km investigated by Johnson *et al.* (2000), very similar results were reported by them (their Fig. 5). For the past NPC (maximum extent), the trend is the same, but f_{iso} is generally somewhat larger. As we will discuss below in more detail, this behaviour has a distinct impact on the ice dynamics. The larger H_1 , the smaller the lithospheric deflection,

modulus, $\eta_{\text{um}} / \mu_{\text{um}}$ [see Eq. (4)], which is 218.5 yr for our values (Table 2) and 316.9 yr for those of Johnson *et al.* (2000).

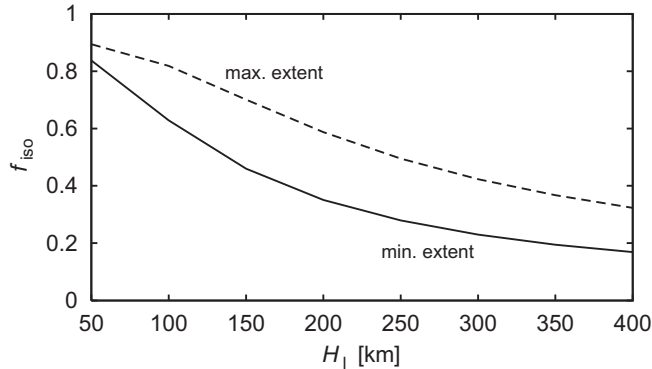


Figure 5: Computed fraction of isostatic compensation, f_{iso} , for the centre of the NPC (north pole) as a function of lithosphere thickness, H_1 , for minimum ice extent at present and maximum ice extent at $t = -650$ kyr.

the thinner the NPC for given surface topography, the slower the ice flow and the smaller the accumulation and ablation rates.

We will see below that the simulation with $H_1 = 100$ km, $q_{\text{geo}}^s = 25$ mW m $^{-2}$ is a probable scenario under the assumptions of this study. Therefore, this simulation shall now be discussed exemplarily in some detail. Figures 6 and 7 show the ice and lithosphere surfaces, the velocity and temperature fields and the surface velocities and accumulation-ablation rates for cross-sections across the centre (north pole) of the NPC and present and past ($t = -650$ kyr) conditions, respectively. A distinct lithosphere depression can be recognized. At the centre, it reaches 63% of full isostatic compensation for the present volume minimum and 82% for the past maximum (see also Fig. 5). The flow field shows the typical downward-and-outward pattern for a grounded ice body and reaches maximum surface velocities, $v_{s,\text{max}}$, of 2.96 mm yr $^{-1}$ at present and 66.5 mm yr $^{-1}$ in the past. Correspondingly, the maximum accumulation rates, S_{max} , and ablation rates, M_{max} , are 0.13 mm w.e. yr $^{-1}$ and 0.11 mm w.e. yr $^{-1}$, resp., for the present, compared to 2.57 mm w.e. yr $^{-1}$ and 0.41 mm w.e. yr $^{-1}$, resp., in the past. These large differences, which occur periodically over the obliquity cycles due to varying ice volume and surface temperature, reflect the “stop-and-go-type dynamics” of the NPC, a behaviour that has already been described by Greve (2000a).

In sharp contrast to the advection-controlled temperature fields of terrestrial ice sheets, the temperature field of the Martian NPC is mainly controlled by heat conduction, so that the temperature increases regularly with depth with a gradient determined by the geothermal heat flux. This is a direct consequence of the very small flow velocities. The maximum basal temperature relative to pressure melting is -61.4°C at present and -40.6°C in the past.

Figure 8 displays the computed present values of S_{max} and M_{max} for the parameter

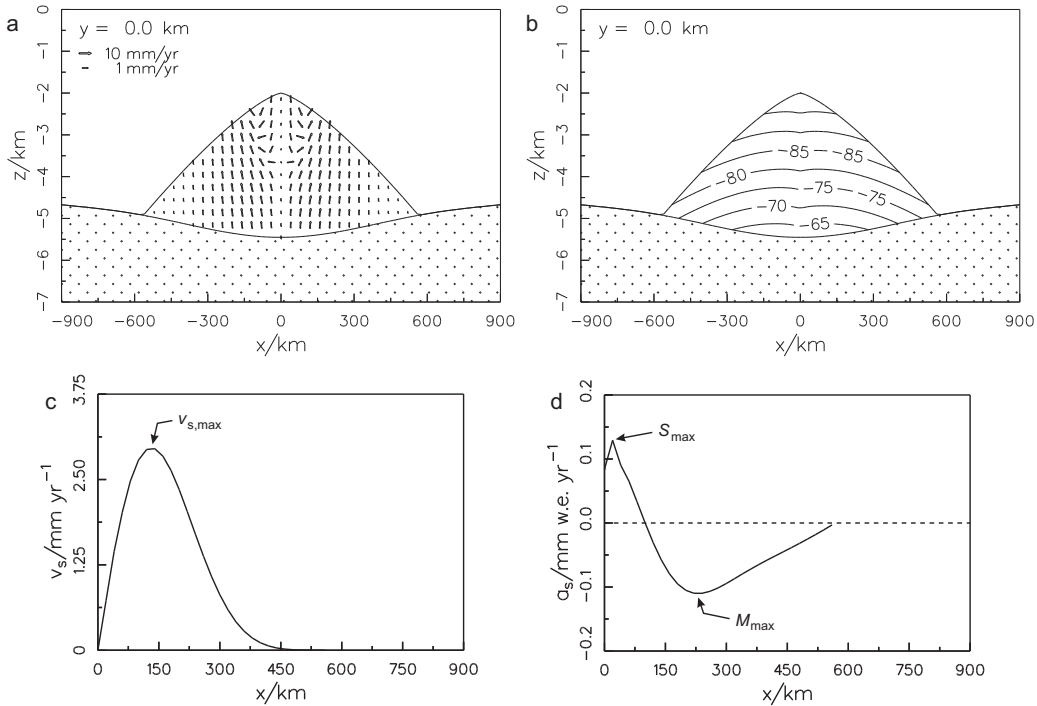


Figure 6: Simulation with parameters $H_1 = 100$ km, $q_{\text{geo}}^s = 25$ mW m $^{-2}$; minimum extent at present. (a) flow-velocity field, (b) temperature field (relative to pressure melting, in $^{\circ}\text{C}$) for a cross-section across the north pole $(x, y) = (0, 0)$ (x, y span the horizontal plane). (c) surface velocity, (d) accumulation-ablation rate for a flowline from the north pole $(x, y) = (0, 0)$ to the margin. Maximum values $v_{s,\text{max}}$, S_{max} and M_{max} are indicated.

space of H_1 and q_{geo}^s . Both values increase with decreasing H_1 (enhanced ice flow due to increased ice thickness) and increasing q_{geo}^s (enhanced ice flow due to increased ice temperature). S_{max} and M_{max} vary between almost 10 mm w.e. yr $^{-1}$ and zero; the reason for S_{max} becoming zero for some of the simulations with $q_{\text{geo}}^s \leq 20$ mW m $^{-2}$ is that the simulated ice flow is so slow in these cases that the whole surface of the NPC, which was larger in the past [Eq. (8), Fig. 2], has a negative mass balance. Greve (2000a) extensively discussed the problem of independent estimates of these quantities mainly from atmospheric considerations and argued that, despite large uncertainties, the order of 0.1 mm w.e. yr $^{-1}$ is a likely range.² Following this reasoning, we define an interval varying by a factor of ten around 0.1 mm w.e. yr $^{-1}$ ($0.1/\sqrt{10} \dots 0.1 \times \sqrt{10}$ mm w.e. yr $^{-1}$) as the target range for the computed present values of S_{max} and M_{max} (shaded areas in Fig. 8). Evidently, the resulting limitations for possible combinations of H_1 and q_{geo}^s are

²This value can be made plausible as follows: The mean water-vapour abundance in the atmosphere of Mars is of the order of 10 precipitable micrometers, compared to some centimeters on Earth (Jakosky and Haberle 1992). If we assume that this ratio ($\sim 1/3000$) transfers to accumulation/ablation rates and use the terrestrial Greenland ice sheet with on average ~ 300 mm w.e. yr $^{-1}$ for comparison, we obtain ~ 0.1 mm w.e. yr $^{-1}$ for the Martian NPC.

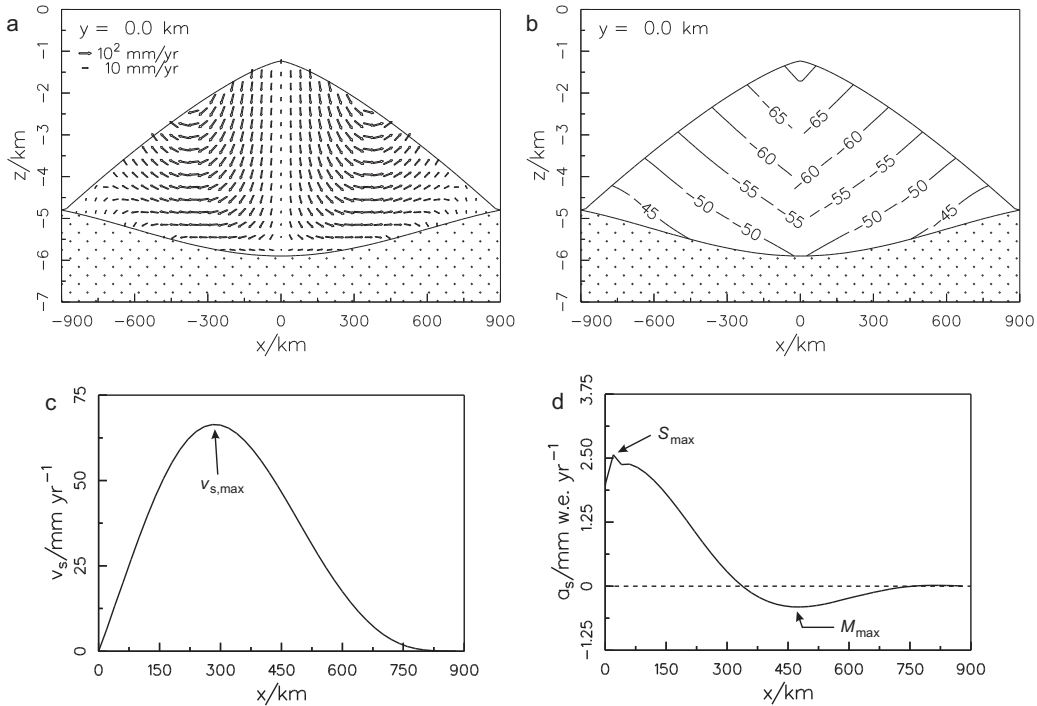


Figure 7: Simulation with parameters $H_1 = 100$ km, $q_{geo}^s = 25$ mW m⁻²; maximum extent at $t = -650$ kyr. (a) flow-velocity field, (b) temperature field (relative to pressure melting, in °C) for a cross-section across the north pole $(x, y) = (0, 0)$ (x, y span the horizontal plane). (c) surface velocity, (d) accumulation-ablation rate for a flowline from the north pole $(x, y) = (0, 0)$ to the margin. Maximum values $v_{s,max}$, S_{max} and M_{max} are indicated.

stronger due to the target range of S_{max} than due to that of M_{max} , and the intersection of both target ranges is essentially equal to that of S_{max} . Since this intersection covers all considered values of H_1 , a constraint on H_1 does not arise. However, possible values of q_{geo}^s are limited to the interval 15...36 mW m⁻².

By using the additional relation (Fig. 3) between q_{geo}^s and H_1 with the depleted crust, both quantities can be further constrained. The intersection of this relation with the target ranges of S_{max} and M_{max} yields rather small “allowed” intervals of ca. $H_1 = 80 \dots 120$ km and $q_{geo}^s = 20 \dots 30$ mW m⁻². This justifies the parameters $H_1 = 100$ km, $q_{geo}^s = 25$ mW m⁻² chosen for the exemplary simulation discussed above. However, it must be kept in mind that relation (21) depends on a number of parameters which can only be estimated roughly, so that these additional constraints of q_{geo}^s and H_1 are fairly uncertain.

A lithosphere thickness of ca. 100 km and a low heat source density would agree well with the results from mantle differentiation modelling for the northern lowlands (Breuer *et al.* 1993). Thicknesses of less than 100 km have been suggested from analyses of MGS gravity and topography data (Johnson *et al.* 2000, Zuber *et al.* 2000). However, such estimates are based on topographic features formed in the distant past (≥ 1000 Myr before

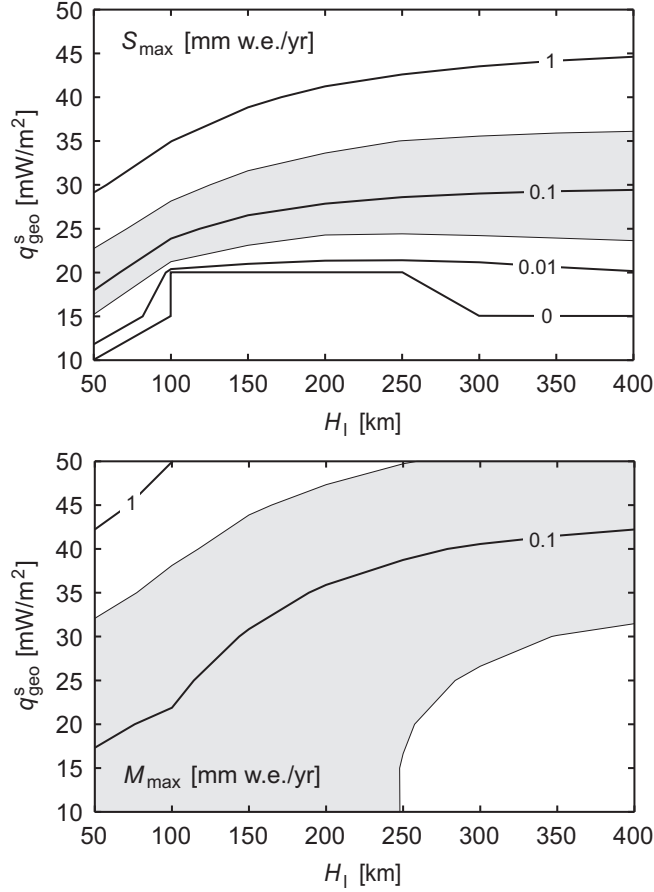


Figure 8: Computed maximum present accumulation and ablation rates at the ice surface, S_{max} and M_{max} , as functions of lithosphere thickness, H_1 , and geothermal heat flux, q_{geo}^s . Shaded areas mark the target ranges of $\mathcal{O}(0.1 \text{ mm w.e. yr}^{-1})$.

present) and, thus, represent rheological conditions for higher subsurface temperatures than today and not the present state (Banerdt *et al.* 1992).

The parameter space of H_1 and q_{geo}^s yields a wide range of possible ice-flow velocities. Fig. 9 shows that the maximum surface velocity varies between 0.11 mm yr^{-1} and 144 mm yr^{-1} , which includes everything between essentially stagnant and distinctly flowing ice. Restriction to the intersection of the target ranges of S_{max} and M_{max} narrows this range to the interval of $1 \dots 5 \text{ mm yr}^{-1}$. This is four to five orders of magnitude smaller than the ice flow in the terrestrial ice sheets of Antarctica and Greenland (see also the above discussion of the stop-and-go-type dynamics).

For all simulations and all times, the basal temperatures are far below pressure melting. For the present, the maximum basal temperature reaches values between -78°C and -34°C and within the intersection of the target ranges of S_{max} and M_{max} it varies between -70°C and -55°C (Fig. 10; all values relative to pressure melting). This means that, provided the melting point of the material of the NPC is close to that of pure ice, it is very unlikely

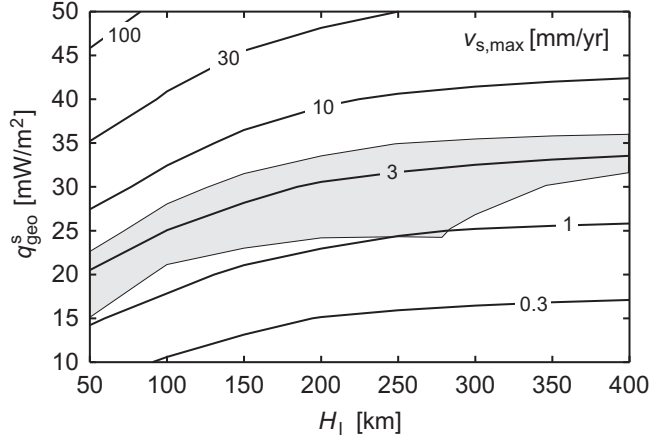


Figure 9: Computed maximum present flow velocity at the ice surface, $v_{s,max}$, as a function of lithosphere thickness, H_1 , and geothermal heat flux, q_{geo}^s . The shaded area marks the intersection of the target ranges of S_{max} and M_{max} (Fig. 8).

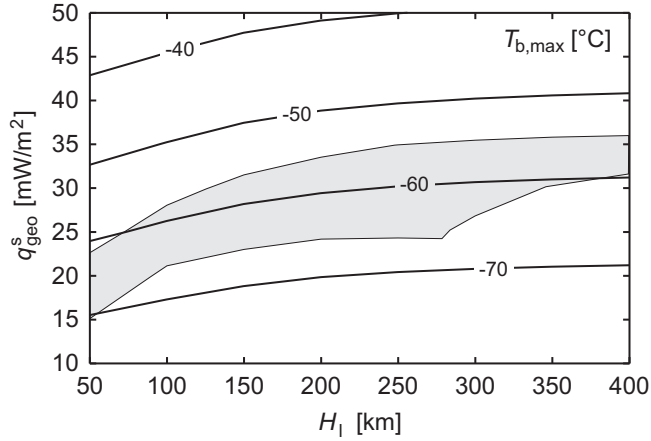


Figure 10: Computed maximum present basal ice temperature relative to pressure melting, $T_{b,max}$, as a function of lithosphere thickness, H_1 , and geothermal heat flux, q_{geo}^s . The shaded area marks the intersection of the target ranges of S_{max} and M_{max} (Fig. 8).

that liquid water is present at the base of the ice mass. However, recent investigations in Antarctica have shown that ponds of liquid water exist at temperatures down to -50°C due to dissolved CaCl_2 , and some saline soils contain a few percent of liquid water down to even -70°C (Wynn-Williams, pers. comm. 2000). Under comparable conditions, liquid water may thus be found at the base of the NPC despite the low temperatures, and, therefore, a chance remains that this region may serve as a potential habitat for lifeforms.

Greve (2000a) extensively discussed the sources of uncertainty for ice-flow simulations of the NPC, such as density, material behaviour and stiffening due to dust content. As already pointed out by Durham (1998), it was concluded that these factors [and also the possible occurrence of induced anisotropy of the ice grains, which may modify the isotropic

flow law (1), see e.g. Svendsen and Hutter (1996)] are of secondary importance compared to the influence of uncertainties of the temperature field, which affects the ice flow via the exponentially temperature-dependent flow-rate factor $A(T')$ in Eq. (1). Apart from the surface temperature, the temperature field in the lower parts of the NPC (where most of the deformation takes place) is controlled by the geothermal heat flux and the heat conductivity of the NPC material. The uncertainty of the geothermal heat flux is assessed here by varying it over the range of plausible values. For the heat conductivity, we use the value for pure ice in terrestrial ice sheets (Table 1); however, it may be distinctly smaller due to mixed-in dust, which consequently would warm the lower parts of the NPC (Clifford 1987, Larsen and Dahl-Jensen 2000).

Therefore, the influence of dust content in the NPC is now assessed explicitly by repeating the above reference simulation with $H_1 = 100$ km, $q_{\text{geo}}^s = 25$ mW m⁻² for dust volume fractions $\varphi = 0.1, 0.2$ and 0.5 . The density, ρ , and heat conductivity, λ , of the ice-dust mixture are computed as volume-fraction-weighted averages of the values for pure ice and crustal material, and the flow-enhancement (or for this application rather flow-obstruction) factor, E , in the flow law (1) is by Durham (1998), based on laboratory measurements of the deformation of ice-dust compounds:

$$\begin{aligned}\rho &= (1 - \varphi)\rho_i + \varphi\rho_c, \\ \lambda &= (1 - \varphi)\lambda_i + \varphi\lambda_c, \\ E &= e^{-2\varphi}.\end{aligned}\tag{23}$$

Results for present conditions and $\varphi = 0 / 0.1 / 0.2 / 0.5$ are as follows: Maximum surface velocity $v_{s,\text{max}} = 2.96 / 2.40 / 5.13 / 27.24$ mm yr⁻¹, maximum accumulation rate $S_{\text{max}} = 0.13 / 0.078 / 0.28 / 1.83$ mm w.e. yr⁻¹, maximum ablation rate $M_{\text{max}} = 0.11 / 0.13 / 0.17 / 0.52$ mm w.e. yr⁻¹, maximum basal temperature relative to pressure melting $T_{b,\text{max}} = -61.4 / -58.8 / -56.5 / -51.5^\circ\text{C}$. Basal warming due to decreasing heat conductivity is clearly visible, and leads to distinctly enhanced ice flow for $\varphi \geq 0.2$. By contrast, for $\varphi = 0.1$ the direct stiffening effect described by Eq. (23c) predominates, so that in this case ice flow is reduced. Evidently, for $\varphi \leq 0.2$ (20% dust content at maximum), $v_{s,\text{max}}$, S_{max} and M_{max} are within a factor two of their values for pure ice, and $T_{b,\text{max}}$ is altered by less than 5°C, which can be regarded as an acceptable uncertainty range concerning the principle nature of our study. For a larger dust content of $\varphi > 0.2$, a possibility which cannot be excluded at the present state of knowledge, the deviations increase quickly, so that our results would be largely invalidated under such circumstances.

As far as the uncertainty of the physical parameters for the ground model (Table 2) is concerned, the viscosity of the upper mantle does not affect our results as long as it is less

than 10^{22} Pa s (see discussion above). The system is most sensitive to variations of the lithosphere thickness, $H_1 = H_c + H_{ml}$. This is because, in the thin-plate approximation, the flexural rigidity of the lithosphere, K_1 , is given by

$$K_1 = \frac{\mu_1 H_1^3}{6(1 - \nu_1)} = \frac{\mu_1(3\kappa_1 + \mu_1)H_1^3}{3(3\kappa_1 + 4\mu_1)} \quad (24)$$

[e. g., Marguerre and Woernle (1969); $\nu_1 = (3\kappa_1 - 2\mu_1)/(6\kappa_1 + 2\mu_1)$ is Poisson's ratio]. Even though we do not apply the thin-plate approximation here and account for two different elastic plates (crust, mantle lithosphere), this quantity controls approximately the vertical displacement of the lithosphere. Evidently, K_1 depends most strongly on H_1 , which we have varied by almost one order of magnitude in the plausible range of values, so that the effect of reasonable variations of other parameters is covered as well.

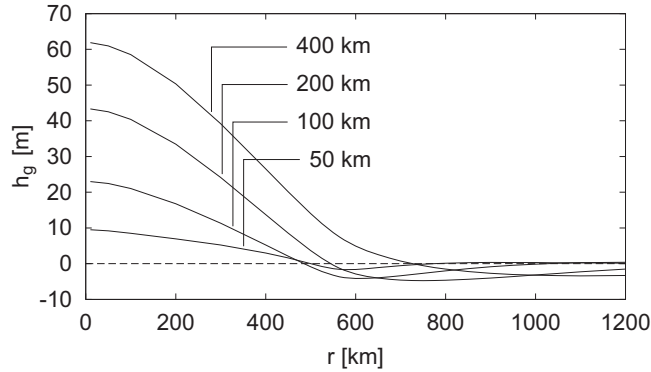


Figure 11: Computed present vertical geoid displacement, h_g , as a function of radial distance from the north pole, r , for lithosphere thicknesses of $H_1 = 50$ km, 100 km, 200 km, 400 km.

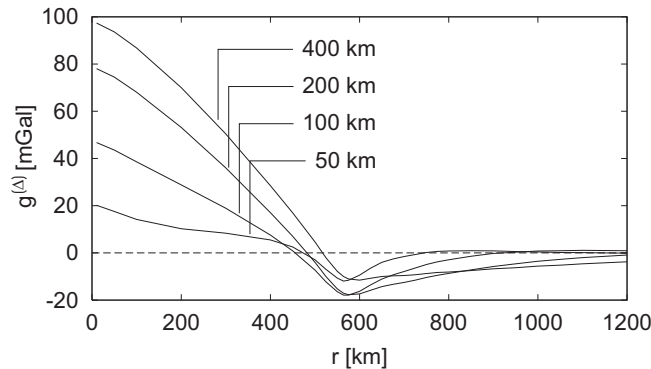


Figure 12: Computed present free-air gravity anomaly, $g^{(\Delta)}$, as a function of radial distance from the north pole, r , for lithosphere thicknesses of $H_1 = 50$ km, 100 km, 200 km, 400 km.

The gravity signal due to the combined effect of the mass of the NPC and its isostatic compensation is displayed in Figs. 11 and 12, which show the present vertical geoid dis-

placement, h_g (positive upward), and the present free-air gravity anomaly, $g^{(\Delta)}$ (downward component of the vector quantity $\mathbf{g}^{(\Delta)}$ introduced in Sect. 2.2), respectively. As expected, both signals increase with increasing lithosphere thickness due to the smaller isostatic compensation (Fig 5). The quantities h_g and $g^{(\Delta)}$ take maximum values of some 10 m and some 10 mGal near the center of the NPC and become slightly negative near the margin. As the gravity field derived from tracking the orbit of the MGS spacecraft has an accuracy of approximately 10 mGal at the poles (Zuber *et al.* 2000), the signal of the NPC can in principle be resolved. However, Johnson *et al.* (2000), whose computed gravity anomalies agree well with our findings (see their Fig. 6), showed that the measured free-air gravity anomaly varies by more than 250 mGal within 80°N and the correlation to the topography of the NPC is actually very poor, so that the signal is probably hidden by disturbances of a different origin, such as mass anomalies in the ground. Interestingly, the correlation appears to be distinctly better for the south polar cap (Smith *et al.* 1999b).

5 Conclusion

The main results of the present study are as follows:

- Present accumulation/ablation rates of $\mathcal{O}(0.1 \text{ mm w.e. yr}^{-1})$ at the surface of the NPC, which can be roughly estimated from atmospheric considerations, are consistent with the modelled ice flow.
- Present basal temperatures are far below pressure melting. Therefore, liquid water can be expected only for high salinities.
- Ice-flow velocities and accumulation/ablation rates for past obliquity maxima are one to two orders of magnitude larger than present ones (stop-and-go-type dynamics).
- Values for the present geothermal heat flux at the top of the crust that are consistent with our target ranges for present accumulation/ablation rates vary between 15 and 36 mW m^{-2} . For the thickness of the rheological lithosphere below the NPC, the full investigated range from 50 to 400 km is possible.
- By employing additionally the relation between the surface heat flux and the lithosphere thickness for the more realistic depleted crust (Fig. 3), these quantities may be further constrained to 20–30 mW m^{-2} and 80–120 km, respectively. However, this must be taken with care due to parameter uncertainties.

- Provided that the viscosity of the upper mantle is not more than an order of magnitude larger than the terrestrial value ($\sim 10^{21}$ Pa.s), the mantle behaves as an inviscid fluid for the considered temporal variation and spatial extent of the ice load.
- The combined present free-air gravity signal of the NPC and the isostatic depression of the underlying ground is some 10 mGal. However, the measured signal shows variations of much larger amplitudes, so that the signal of the NPC and their compensation is hidden by mass anomalies of a different origin.

A shortcoming of the present work is that the prescribed climate history (surface temperature, ice extent) is based on very little information. For future work, it is therefore promising to include the atmospheric conditions in the modelling approach and to use the orbital elements (obliquity, eccentricity) directly as forcing functions. This can be achieved either by rather simple energy-balance considerations at the surface of the NPC (Larsen and Dahl-Jensen 2000), or by coupling a general-circulation model (GCM) for the Martian atmosphere (cf. Lewis *et al.* 1999 and references therein). Within a recently launched project funded by the German Science Foundation DFG (Keller *et al.* 2001), these ideas will be pursued.

Acknowledgements

This paper is the outcome of a presentation held on the “Second International Conference on Mars Polar Science and Exploration” (Reykjavík, Iceland, August 21–25, 2000). We wish to thank the organizers, in particular S. M. Clifford and T. Thorsteinsson, for their great commitment, which led to a lively and fruitful conference. Further, this paper benefited from the comments of K. Hutter and the reviews of T. Thorsteinsson and an anonymous referee.

References

- Banerdt, W. B., M. P. Golombek and K. L. Tanaka 1992. Stress and tectonics on Mars. In *Mars* (H. H. Kieffer, B. M. Jakosky, C. W. Snyder and M. S. Matthews, Eds.), pp. 249–297. Univ. of Arizona Press, Tucson.
- Bass, D. S. and D. A. Paige 1999. Evidence for the possible accumulation of ice at the north pole of Mars. Abstract, Fifth International Conference on Mars, Pasadena.
- Breuer D., T. Spohn and U. Wüllner 1993. Mantle differentiation and the crustal dichotomy of Mars. *Planet. Space Sci.* **41**, 269–283.

- Byrne, S. and B. C. Murray 2002. North polar stratigraphy and the paleo-erg of Mars. *J. Geophys. Res.* **107**, 5044, doi: 10.1029/2001JE001615.
- Clifford, S. M. 1987. Polar basal melting on Mars. *J. Geophys. Res.* **92**, 9135–9152.
- Clifford, S. M., D. Crisp, D. A. Fisher, K. E. Herkenhoff, S. E. Smrekar, P. C. Thomas, D. D. Wynn-Williams, R. W. Zurek, J. R. Barnes, B. G. Bills, E. W. Blake, W. M. Calvin, J. M. Cameron, M. H. Carr, P. R. Christensen, B. C. Clark, G. D. Clow, J. A. Cutts, D. Dahl-Jensen, W. B. Durham, F. P. Fanale, J. D. Farmer, F. Forget, K. Gotto-Azuma, R. Grard, R. M. Haberle, W. Harrison, R. Harvey, A. D. Howard, A. P. Ingersoll, P. B. James, J. S. Kargel, H. H. Kieffer, J. Larson, K. Lepper, M. C. Malin, D. J. McCleese, B. Murray, J. F. Nye, D. A. Paige, S. R. Platt, J. J. Plaut, N. Reeh, J. W. Rice, D. E. Smith, C. R. Stoker, K. L. Tanaka, E. Mosley-Thompson, T. Thorsteinsson, S. E. Wood, A. Zent, M. T. Zuber and H. J. Zwally 2000. The state and future of Mars polar science and exploration. *Icarus* **144**, 210–242.
- Durham, W. B. 1998. Factors affecting the rheologic properties of Martian polar ice. *First International Conference on Mars Polar Science and Exploration*, LPI Contribution No. 953, pp. 8–9. Lunar and Planetary Institute, Houston.
- Greve, R. 2000a. Waxing and waning of the perennial north polar H₂O ice cap of Mars over obliquity cycles. *Icarus* **144**, 419–431.
- Greve, R. 2000b. *Large-scale glaciation on Earth and on Mars*. Habilitation thesis, Department of Mechanics, Darmstadt University of Technology, 274pp.
- Greve, R., M. Weis and K. Hutter 1998. Palaeoclimatic evolution and present conditions of the Greenland Ice Sheet in the vicinity of Summit: An approach by large-scale modelling. *Paleoclimates* **2**, 133–161.
- Herkenhoff, K. E. and J. J. Plaut 2000. Surface ages and resurfacing rates of the polar layered deposits on Mars. *Icarus* **144**, 243–253.
- Jakosky, B. M. and R. M. Haberle 1992. The seasonal behavior of water on Mars. In *Mars* (H. H. Kieffer, B. M. Jakosky, C. W. Snyder and M. S. Matthews, Eds.), pp. 969–1016. Univ. of Arizona Press, Tucson.
- Jakosky, B. M., B. G. Henderson and M. T. Mellon. 1993. The Mars water cycle at other epochs: Recent history of the polar caps and layered terrain. *Icarus* **102**, 286–297.
- Johnson, C. L., S. C. Solomon, J. W. Head, R. J. Phillips, D. E. Smith and M. T. Zuber 2000. Lithospheric loading by the northern polar cap on Mars. *Icarus* **144**, 313–328.
- Keller, H. U., D. Titov, B. Grieger, K. Fraedrich and R. Greve 2001. Investigation of the current and ancient Martian climate, its stability and mechanisms of changes by means of a modular planet simulator model. Proposal to the German Science Foundation DFG.
- Kieffer, H. H. and A. P. Zent 1992. Quasi-periodic climate change on Mars. In *Mars* (H. H. Kieffer, B. M. Jakosky, C. W. Snyder and M. S. Matthews, Eds.), pp. 1180–1218. Univ. of Arizona Press, Tucson.
- Klemann, V. and D. Wolf 1999. Implications of a ductile crustal layer for the deformation caused by the Fennoscandian ice sheet. *Geophys. J. Int.* **139**, 216–226.
- Klemann, V., P. Wu and D. Wolf 2003. Compressible viscoelasticity: Stability of solutions for homogeneous plane earth models. *Geophys. J. Int.* (in press).

- Larsen, J. and D. Dahl-Jensen 2000. Interior temperatures of the northern polar cap on Mars. *Icarus* **144**, 456–462.
- Laskar, J., B. Levrard and J. F. Mustard 2002. Orbital forcing of the martian polar layered deposits. *Nature* **419**, 375–377.
- Lewis, S. R., M. Collins, P. L. Read, F. Forget, F. Hourdin, R. Fournier, C. Hourdin, O. Talagrand and J.-P. Huot 1999. A climate database for Mars. *J. Geophys. Res.* **104**, 24177–24194.
- Marguerre, K. and H.-T. Woernle 1969. *Elastic plates*. Blaisdell Publishing Company, Waltham, Mass., etc., 214 pp.
- McKenzie, D. and M. J. Bickle 1988. The volume and composition of melt generated by extension of the lithosphere. *J. Petrol.* **26**, 625–679.
- Meissner, R. O. and U. R. Vetter 1979. Relationship between the seismic quality factor Q and the effective viscosity η^* . *J. Geophys.* **45**, 147–158.
- Nye, J. F. 2000. A flow model for the polar caps of Mars. *J. Glaciol.* **46**, 438–444.
- Parmentier, E. M. and O. Grasset 1998. Thermal convection in a volumetrically heated, infinite Prandtl number fluid with strongly temperature-dependent viscosity: Implications for planetary thermal evolution. *J. Geophys. Res.* **103**, 18171–18181.
- Paterson, W. S. B. 1994. *The physics of glaciers*. Third edition. Oxford, etc., Pergamon Press, 480 pp.
- Schubert, G., S. C. Solomon, D. L. Turcotte, M. J. Drake and N. H. Sleep 1992. Origin and thermal evolution of Mars. In *Mars* (H. H. Kieffer, B. M. Jakosky, C. W. Snyder and M. S. Matthews, Eds.), pp. 147–183. Univ. of Arizona Press, Tucson.
- Smith, D. E., M. T. Zuber, S. C. Solomon, R. J. Phillips, J. W. Head, J. B. Garvin, W. B. Banerdt, D. O. Muhleman, G. H. Pettengill, G. A. Neumann, F. G. Lemoine, J. B. Abshire, O. Aharonson, C. D. Brown, S. A. Hauck, A. B. Ivanov, P. J. McGovern, H. J. Zwally and T. C. Duxbury 1999a. The global topography of Mars and implications for surface evolution. *Science* **284**, 1495–1503.
- Smith, D. E., W. L. Sjogren, G. L. Tyler, G. Balmino, F. G. Lemoine and A. S. Konopliv 1999b. The gravity field of Mars: Results from Mars Global Surveyor. *Science* **286**, 94–97.
- Sohl, F. and T. Spohn 1997. The interior structure of Mars: Implications from SNC meteorites. *J. Geophys. Res.* **102**, 1613–1635.
- Solomon, S. C. and J. W. Head 1990. Heterogeneities in the thickness of the elastic lithosphere of Mars: Constraints on heat flow and internal dynamics. *J. Geophys. Res.* **95**, 11073–11083.
- Spohn, T., F. Sohl and D. Breuer 1998. Mars. *Astron. Astrophys. Rev.* **8**, 181–235.
- Svendsen, B. and K. Hutter 1996. A continuum approach for modelling induced anisotropy in glaciers and ice sheets. *Ann. Glaciol.* **23**, 262–269.
- Thomas, P., S. Squyres, K. Herkenhoff, A. Howard and B. Murray 1992. Polar deposits of Mars. In *Mars* (H. H. Kieffer, B. M. Jakosky, C. W. Snyder and M. S. Matthews, Eds.), pp. 767–795. Univ. of Arizona Press, Tucson.
- Touma, J. and J. Wisdom 1993. The chaotic obliquity of Mars. *Science* **259**, 1294–1297.

- Ward, W. R. 1992. Long-term orbital and spin dynamics of Mars. In *Mars* (H. H. Kieffer, B. M. Jakosky, C. W. Snyder and M. S. Matthews, Eds.), pp. 298–320. Univ. of Arizona Press, Tucson.
- Wolf, D. 1985a. The normal modes of a layered, incompressible Maxwell half-space. *J. Geophys.* **57**, 106–117.
- Wolf, D. 1985b. The normal modes of a uniform, compressible Maxwell half-space. *J. Geophys.* **56**, 100–105.
- Wu, P. and W. R. Peltier 1982. Viscous gravitational relaxation. *Geophys. J. R. Astr. Soc.* **70**, 435–485.
- Wüllner, U. and H. Harder 1998. Convection underneath a crust inhomogeneously enriched in heat sources: application to martian mantle dynamics. *Phys. Earth Planet. Int.* **109**, 129–150.
- Zuber, M. T., D. E. Smith, S. C. Solomon, J. B. Abshire, R. S. Afzal, O. Aharonson, K. Fishbaugh, P. G. Ford, H. V. Frey, J. B. Garvin, J. W. Head, A. B. Ivanov, C. L. Johnson, D. O. Muhleman, G. A. Neumann, G. H. Pettengill, R. J. Phillips, X. Sun, H. J. Zwally, W. B. Banerdt and T. C. Duxbury 1998. Observations of the north polar region of Mars from the Mars Orbiter Laser Altimeter. *Science* **282**, 2053–2060.
- Zuber, M. T., S. C. Solomon, R. J. Phillips, D. E. Smith, G. L. Tyler, O. Aharonson, G. Balmino, W. B. Banerdt, J. W. Head, C. L. Johnson, F. G. Lemoine, P. J. McGovern, G. A. Neumann, D. D. Rowlands and S. Zhong 2000. Internal structure and early thermal evolution of Mars from Mars Global Surveyor topography and gravity. *Science* **287**, 1788–1793.